Chem

Article

Visualization of CO formation at the triple-phase boundary in gas diffusion electrodes for ecCO_2RR

Graphical abstract

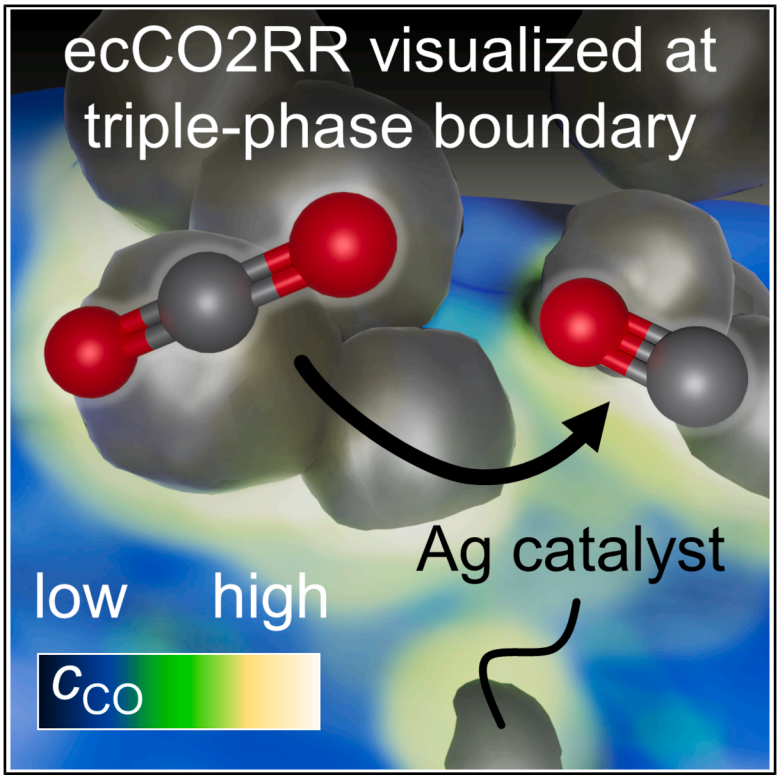

Highlights

- Microfluidic gas diffusion electrode for monitoring electrochemical CO_2 reduction
- *In operando* detection of reaction locations for CO and H_2 formation
- Highest CO concentrations near triple-phase boundary
- H_2 formation independent from flooding degree of catalyst layer

Authors

Sebastian Brosch, Eike Häger, Ole Frank, Patrick Scholz, Wenzel Plischka, Matthias Wessling

Correspondence

sebastian.brosch@rwth-aachen.de (S.B.), manuscripts.cvt@avt.rwth-aachen.de (M.W.)

In brief

Electrochemical CO_2 reduction can mitigate the consequences of human-made climate change. The process is not yet fully understood. Mainly, the distribution of reaction locations for the desired reactions and the side reactions within the gas diffusion electrodes used for CO_2 reduction are not understood. We present a microfluidic model capable of tracing zones of reactivity for CO and H_2 within the catalyst layer of a gas diffusion electrode to fundamentally understand the process of electrochemical CO_2 reduction.

Brosch et al., 2025, Chem *11*, 102582
October 9, 2025
https://doi.org/10.1016/j.chempr.2025.102582

CellPress

Please cite this article in press as: Brosch et al., Visualization of CO formation at the triple-phase boundary in gas diffusion electrodes for ecCO2RR, Chem (2025), https://doi.org/10.1016/j.chempr.2025.102582

Chem

CellPress
OPEN ACCESS

Article

Visualization of CO formation at the triple-phase boundary in gas diffusion electrodes for ecCO$_2$RR

Sebastian Brosch,[1,3,*] Eike Häger,[1] Ole Frank,[1] Patrick Scholz,[1] Wenzel Plischka,[1] and Matthias Wessling[1,2,*]
[1]Chemical Process Engineering, RWTH Aachen University, Forckenbeckstr. 51, Aachen 52074, North Rhine-Westphalia, Germany
[2]DWI-Leibniz Institute for Interactive Materials, Forckenbeckstr. 50, Aachen 52074, North Rhine-Westphalia, Germany
[3]Lead contact
*Correspondence: sebastian.brosch@rwth-aachen.de (S.B.), manuscripts.cvt@avt.rwth-aachen.de (M.W.)
https://doi.org/10.1016/j.chempr.2025.102582

THE BIGGER PICTURE Electrochemical processes hold significant potential for storing excess renewable energy while simultaneously converting pollutants into valuable feedstock chemicals. In the context of electrochemical CO_2 reduction, CO_2 is transformed into CO, a critical precursor for numerous chemical processes.

This research focuses on a detailed investigation of the conditions and specific locations within an electrochemical cell where the desired product, CO, is formed. The findings aim to guide future advancements in cell design, optimization of catalyst materials, and determination of ideal process conditions.

SUMMARY

Electrochemical CO_2 reduction represents a promising technology for mitigating the impact of greenhouse gas emissions, particularly CO_2. Gas diffusion electrodes (GDEs) are widely utilized in this process. Although CO_2 reduction has been successfully demonstrated on small scales with various catalysts, the role of the wetting state of the catalyst layer in GDEs remains poorly understood. This factor significantly influences current density and faradaic efficiency. However, two fundamental questions persist: where within the electrode does the desired reaction occur, and what operating state should be targeted for optimizing performance? In this study, we employ a microfluidic electrolyzer to visualize and selectively identify reaction zones producing CO, the desired product. This approach enables the characterization of reactivity across different states of the electrode, revealing the impact of catalyst-layer wetting on product selectivity. Together with our previous research on GDEs, these findings provide a comprehensive understanding of electrochemical CO_2 reduction.

INTRODUCTION

Electrochemical CO_2 reduction

Electrochemical CO_2 reduction (ecCO$_2$RR) is a critical technology for reducing greenhouse gas emissions and mitigating the effects of anthropogenic climate change. The development of gas diffusion electrodes (GDEs) has significantly increased the achievable current densities in gas-fed electrolyzers.[1] Despite this progress, the mechanisms and optimal parameters for efficient ecCO$_2$RR remain poorly understood.[2,3] The industrial use of oxygen-depolarized cathodes in chloralkali electrolysis demonstrates the considerable potential of GDEs for gas-fed electrolyzers.[4] Although these systems serve as a valuable platform for understanding and implementing GDEs, further fundamental insights into transport and reaction processes in ecCO$_2$RR are necessary.[5]

GDEs generally consist of a layered structure, including a conductive porous substrate and a catalyst layer (CL) applied on top. The substrate can be composed of materials such as carbon cloth, metal foam, or mesh, whereas the CL typically comprises a metal catalyst combined with an ionomeric binder, such as Nafion.[6] Numerous adaptations and specializations of this configuration have been developed to enhance product selectivity or reduce catalyst usage.[7]

For copper-based GDEs, Möller et al. identified distinct selectivity zones, suggesting that the CL's thickness significantly influences the faradaic efficiency (FE) for different reaction products.[8] The local CO_2 concentration, determined by the CL structure and CO_2 pressure, plays a pivotal role in selectivity, emphasizing the critical importance of mass transport in GDEs.[9] Factors such as pore size and layer thickness affect transport properties, and tuning these parameters enables optimization of electrode composition.[10] However, achieving an ideal electrode design for efficient transport to the reaction sites requires a clear understanding of where desired and undesired reactions occur within or on the GDE.

Please cite this article in press as: Brosch et al., Visualization of CO formation at the triple-phase boundary in gas diffusion electrodes for ecCO$_2$RR, Chem (2025), https://doi.org/10.1016/j.chempr.2025.102582

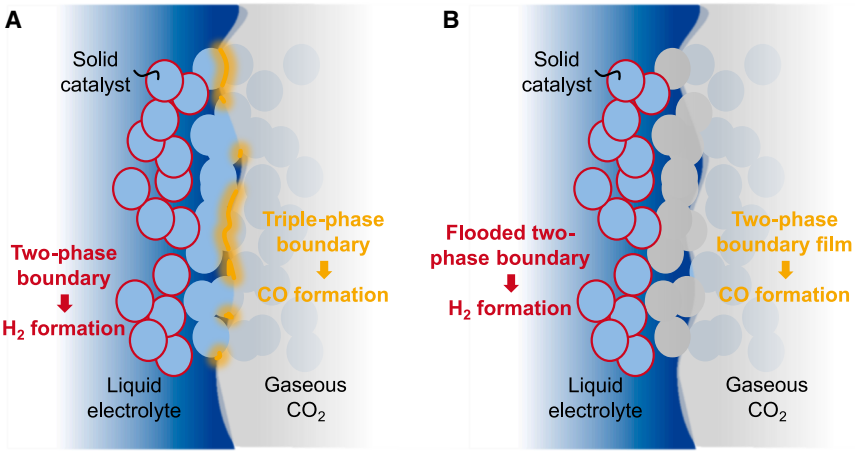

Figure 1. Proposed reaction locations for ecCO$_2$RR and HER within the pore network of silver CLs

(A) ecCO$_2$RR takes place only at the TPB.

(B) A thin film of electrolyte formed near the TPB is the primary reaction location.

Several studies have examined the role of wettability and its influence on selectivity and reaction locations in CO_2 electroreduction. For an in-depth discussion on reactions at triple-phase boundaries (TPBs), we refer to the review by Rabiee et al.[1] The work of Nesbitt et al. provides a broader overview of reactions at two-phase boundaries.[11]

A key point of debate in the scientific community is whether a TPB (catalyst, gas phase, and electrolyte) or a two-phase boundary (solid catalyst and liquid electrolyte) is essential for CO_2 reduction.[12,13] The prevailing hypothesis in much of the literature is that CO_2 reduction occurs at the TPB.[1,14,15] However, other studies present strong evidence suggesting that the governing reaction location is the two-phase boundary, specifically at the interface between the electrolyte-covered catalyst and the liquid phase.[16,17] In this scenario, the reaction zone is reported to exist in close proximity to the catalyst surface, where the mass transport of reactants through the electrolyte is the limiting step.

Supporting this, Nesbitt et al. demonstrated that for ionomer-free metal GDEs, the two-phase boundary between catalyst and electrolyte primarily determines electrode reactivity.[11] These findings underscore the role of electrode wettability in influencing reactivity and selectivity. The ionomer, in particular, plays a significant role because it strongly affects wettability. For instance, hydrophobicity in porous transport layers promotes ecCO$_2$RR, but the same does not necessarily apply to CLs. Studies by Junge Puring et al. showed that modifying CLs with hydrophilic ionomers yielded superior results, further supporting the conclusions of Nesbitt et al.[18] The two proposed distributions are shown schematically in Figure 1.

Overall, managing the liquid phase and preventing electrolyte flooding into the gas side are critical for maintaining selectivity. Factors such as temperature control, ionomer type and quantity, and the choice of solvent in catalyst dispersion significantly affect GDE performance.[19] However, determining optimal reaction conditions is complex because they vary depending on electrode design, electrolyte composition, and catalyst type.

Controlling electrode wetting and CL saturation is a key factor in achieving high FEs.[20,21] Identifying the precise reaction locations within a specific GDE design is essential for optimization. Although no universal answer exists given the variability in electrode designs, gaining a fundamental understanding of these processes can significantly influence electrode development strategies. This knowledge has the potential to reduce the reliance on scarce and expensive precious-metal catalysts, further advancing the efficiency and scalability of ecCO$_2$RR technologies.

There is a clear need for a platform capable of determining reaction locations *in operando* to guide the composition and design of GDE CLs under various conditions and process parameters. In this study, we present a detection system that enables visualization of CO formation within the CL of a microfluidic GDE replica. The microfluidic electrode design allows for the systematic variation of critical parameters, including ionomer content, layer thickness, gas pressure, CO_2 concentration, and electrolyte pressure.

These parameters significantly influence the FE for specific reaction products. This work specifically investigates the effects of the wetting state (i.e., electrolyte distribution and interfacial area), cell potential, and CO_2 transport on reaction performance.

In situ investigation of ecCO$_2$RR

The limited optical access and the microscale to nanoscale dimensions of the system make investigating transport phenomena within a GDE significantly challenging. The electrode is typically integrated into an electrochemical cell, where its porous layer is neither optically accessible nor transparent. Consequently, many studies on GDEs rely on mathematical models or digital reconstructions.[22,23] Although these approaches provide valuable insights into the transport characteristics of specific GDE structures or compositions, direct *in situ* or *in operando* observations offer a more comprehensive understanding of the processes at play.

Experimental techniques are essential for examining the previously mentioned influences on electrochemical processes. Conventional process optimization involves measuring the electrochemical properties of a cell and optimizing parameters such as FE toward CO. However, this approach requires numerous experiments and provides limited insight into the mechanisms occurring within the GDE and its CL. Coupling electrochemical measurements with optical methods can yield additional insights, particularly into phenomena such as electrowetting.[24] Electrowetting refers to the change in surface wettability induced by an applied potential,[25] a critical factor for GDEs as it directly affects the wetting state during operation. Potential-induced wetting has been shown to significantly influence electrode performance.[26]

Several visualization techniques have been developed for analyzing processes at the surface and within GDEs. To

Please cite this article in press as: Brosch et al., Visualization of CO formation at the triple-phase boundary in gas diffusion electrodes for ecCO$_2$RR, Chem (2025), https://doi.org/10.1016/j.chempr.2025.102582

overcome imaging challenges, tomography methods are commonly employed. X-ray or synchrotron imaging has been used for studying the wetting state of silver GDEs[27,28] and the catalytically active states of electrocatalysts[29] *in operando*. Rieder et al. investigated GDE flooding by using elemental analysis and mass spectroscopy on segmented GDEs. They also conducted *operando* studies with X-ray computed tomography but concluded that this technique, although effective, is more costly and time intensive than simpler methods and offers only comparable results.[30]

Recently, Lu et al. introduced optical coherence tomography to visualize fluid distribution within porous electrodes and identify reaction products in different phases.[31] This method provides an excellent overview of phase distribution and offers insights into process conditions favoring CO or H_2 production. However, it lacks the resolution necessary for detecting dissolved reaction products.

For a more detailed understanding of the electrochemical processes within a GDE, parameters such as local pH and pOH must be examined because they provide insights into reactivity and selectivity. Techniques such as scanning electrochemical microscopy,[32] NMR spectroscopy,[33] and fluorescence microscopy[34] can elucidate the effects of micrometer-scale GDE morphology, current distribution, and electrode reactions on electrolyte buffer capacity and pH. Recently, Graf et al. introduced a confocal-microscopy-based method to measure the local concentration and state of charge within a porous electrode.[35]

Combining information on the wetting state with the local microenvironment is ideal for comprehensive analysis. To this end, we previously developed a microfluidic GDE system. Using confocal laser scanning microscopy (CLSM) and fluorescence lifetime imaging microscopy, we analyzed wetting states and local pH values in a realistic representation of a CL for ecCO$_2$RR.[36,37] Unlike other approaches, this microfluidic cell provides rapid, spatiotemporally resolved information on wetting states and local pH values *in operando*.

Building on this work, we now integrate a sensing platform into the microfluidic electrode to detect CO formation and identify active reaction sites while simultaneously monitoring the wetting state and the effects of electrowetting during operation. Although this microfluidic system approximates rather than replicates a full-scale electrochemical cell, it bridges the gap between studies of localized microenvironments and global wetting phenomena. This capability offers valuable insights for optimizing GDE design and performance.

Methods for CO detection

To detect CO in our microfluidic reactor, we drew inspiration from microbiology. In biological applications, sensor molecules are commonly used for detecting specific substances or proteins, enabling the characterization of cells, viruses, or proteins.[38] These sensors typically rely on dyes that adsorb into or react with a target substance, signaling its presence. This principle has been adapted to optical detection methods for non-biological applications, such as gas sensors.[39] For CO detection, two primary approaches can be distinguished: reaction-based detection and coordination-based detection.

In reaction-based systems, CO reacts with a dye or a secondary material, resulting in changes to the dye's fluorescence properties.[40,41] The Tsuji-Trost reaction is frequently employed in such systems.[42–45] Another approach involves the reduction of coordinated Cu^{2+} ions, which alters the fluorescence of the coordinated dye,[46] although this mechanism remains debated in the literature.[47] Reaction-based methods generally rely on the reducing properties of CO. However, these methods are apparently unsuitable for selectively detecting CO in reducing environments, such as the cathode of an electrochemical cell.

Alternatively, CO can be detected through coordination-based methods. These systems use transition-metal complexes whose fluorescence properties change when CO coordinates to the metal center or replaces another ligand.[48] Metals such as iridium, ruthenium, palladium, or rhodium are commonly employed, often with N-heterocyclic carbene ligands functionalized with additional fluorophores to provide the desired fluorescence properties.[49]

Both detection mechanisms typically function as a "turn-on" probe, where fluorescence intensity increases significantly upon interaction with CO. This approach enables simultaneous investigation of wetting behavior and reaction activity: weak fluorescence signals can indicate the wetting state of the electrode, whereas strong signals signify the presence of CO. In this work, we used a known ruthenium-based complex, [Ru(CH=CHPyr-1)Cl(CO)(BTD)(PPh_3)$_2$] (Ru-PBP), to detect and visualize CO.[50] Additionally, we used the dye Texas Red to measure liquid saturation, allowing us to clearly distinguish between activity and liquid saturation.

Overall, the microfluidic electrode combined with a CO-sensitive dye serves as a powerful tool for investigating the effects of process parameters on the selectivity of ecCO$_2$RR. Furthermore, it provides insights into the specific CL locations where the desired CO_2 reduction reactions occur.

RESULTS

All experiments were conducted in a microfluidic electrochemical cell featuring a porous CL composed of silver nanoparticles and a Nafion NS-5 binder. The electrolyte used was potassium bicarbonate. A general schematic and the region of interest for most measurements are shown in Figure 2. Further details on the cell geometry are provided in Figure S7 and in our previous publications on the development of the microfluidic electrolyzer.[36,37]

Using the microfluidic GDE, we successfully detected wetting phenomena and tracked pH values spatiotemporally *in operando*. In this work, we built on these results by systematically investigating voltage-dependent electrowetting and ecCO$_2$RR within the porous CL. We aimed to characterize the specific CL locations where CO formation occurs and identify the key factors influencing selectivity by tracing product formation *in operando*.

Our first objective was to analyze one of the most critical factors affecting the electrode wetting state during operation: electrowetting.[24,26,51] Understanding the potential-dependent wetting state of the electrode is essential for distinguishing between wetting effects caused by the applied potential and mass-transport dynamics during the reaction.

Please cite this article in press as: Brosch et al., Visualization of CO formation at the triple-phase boundary in gas diffusion electrodes for ecCO$_2$RR, Chem (2025), https://doi.org/10.1016/j.chempr.2025.102582

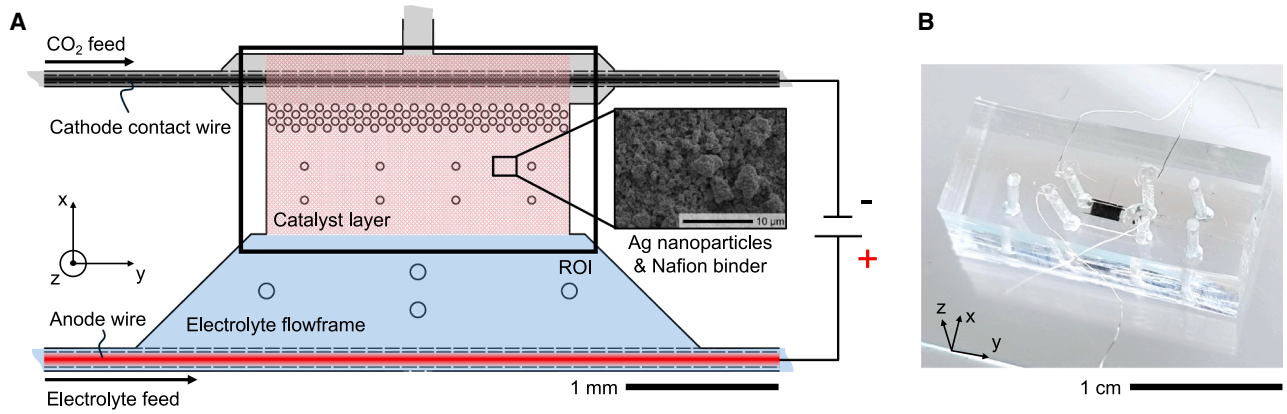

Figure 2. Schematic and photograph of the used microfluidic channel
(A) Schematic layout of flowframe (blue) and CL (red) with contact wires for the cathode and anode.
(B) Photograph of the assembled channel.

Electrowetting

A high interfacial area between liquid and gas is hypothesized to optimize product selectivity, mass transport, and energy efficiency. However, electrowetting, particularly under unstable potentials during constant-current operation, can destabilize the phase boundary. To address this, we investigated the influence of different potentials on the wetting state across various CLs. Our findings indicate that potential-driven electrowetting has the most significant effect in CLs with larger structural defects. Notably, it can also lead to electrolyte breakthrough when a constant overpressure is maintained on the electrolyte side.

We conducted experiments by setting constant-pressure differences between the gas and electrolyte sides while incrementally increasing the applied potential. We monitored the saturation of the CL by using CLSM and conventional fluorescence microscopy. Figure 3 shows the resulting potential-saturation curves for different CLs. Exemplary microscopy images in Figure 3C show a potential-induced breakthrough of electrolyte. To facilitate comparison with pressure-driven saturation measurements, we translated the applied potential into an equivalent pressure contribution. We calculated the total pressure, Δp, for each applied cell voltage, U, at every step by using a modified Lippmann equation (Equation 1; for derivation, see supplemental information section S1).

$$\Delta p = \frac{2\cdot\gamma_{lg}\cdot\cos\theta}{r_{pore}} + \frac{U^2\cdot C_{DL}}{A\cdot r_{pore}} \qquad \text{(Equation 1)}$$

Here, γ_{1g} is the liquid-gas interfacial tension (0.072 N m^{-1} for water was used as a good approximation for our electrolyte), r_{pore} is the average pore radius (see supplemental information section S8), C_{DL} is the double-layer capacitance (see section S2), A is the wetted area, and θ (which we measured to be 110°) is the contact angle between the electrolyte and CL. In all following discussions, we consider only the second term of Equation 1 given that the first describes only the capillary pressure. Thus, we hereafter use the term "equivalent pressure" to describe this second term.

The influence of the electrowetting effect can be understood by analogy to a conventional capacitor, where the electric field generates an equivalent pressure that adds to the capillary pressure described by the Young-Laplace equation. This equivalent pressure depends on several factors. Although the applied voltage has the most significant impact, the wetted area (A) also plays an important role. The electrode's double-layer capacitance, C_{DL}, determined experimentally as detailed in supplemental information section S2, also depends on the wetted area. Here, it is important to consider the role of the ionomer because this changes the capacitance and wettability of the CL. In section S8, we discuss the even distribution of the ionomer and consequently assume an even coverage of the silver particles with Nafion throughout this work.

As the wetted area increases, the effect of electrowetting diminishes. This is because C_{DL} increases at a slower rate with respect to the area than the area itself. At higher interfacial areas and overall saturation levels, the impact of potential-induced wetting becomes less significant because it accounts for only minor relative changes in saturation.

Another critical factor to consider is the so-called saturation voltage ($\tilde{V}$). This is the potential at which the contact angle no longer changes in response to the applied voltage. $\tilde{V}$ can be calculated similarly to the derivation of the equivalent pressure, where the wetting front is described in terms of the Young equation and a plate capacitor model (adapted from Quinn et al.[52]).

$$\tilde{V} = \sqrt{\frac{2\cdot\gamma_{lg}\cdot(\cos\theta - \cos\theta_0)}{C_s}} \qquad \text{(Equation 2)}$$

$$\tilde{V} = \sqrt{\frac{2\cdot 0.072\ \text{Nm}^{-1}\cdot(\cos 0° - \cos 110°)}{0.025\ \text{Fm}^{-2}}} = 2.2\ \text{V} \qquad \text{(Equation 3)}$$

To calculate $\tilde{V}$, we consider two edge cases: a completely wetted surface and a moderate change in the contact angle. For both cases, we use the water contact angle of 110° measured for our catalyst material as θ_0.[37] In the complete

Please cite this article in press as: Brosch et al., Visualization of CO formation at the triple-phase boundary in gas diffusion electrodes for ecCO$_2$RR, Chem (2025), https://doi.org/10.1016/j.chempr.2025.102582

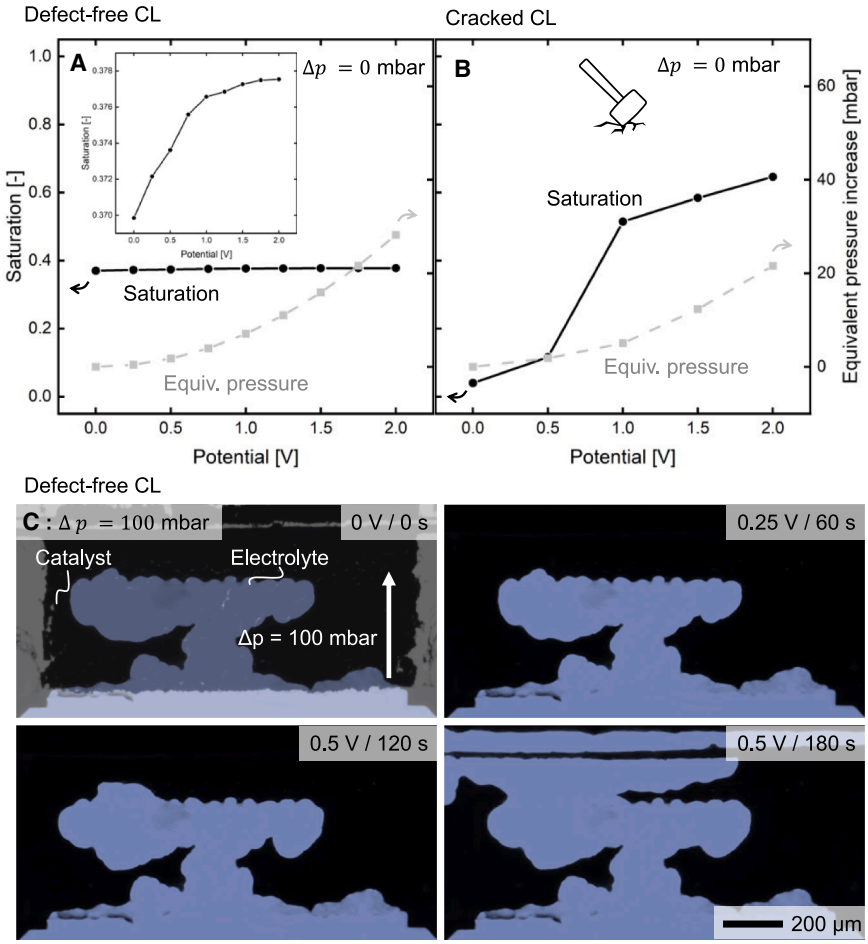

Figure 3. Potential-dependent electrowetting measured in microfluidic GDEs

(A) Saturation and equivalent pressure calculated with Equation 1 in a defect-free CL. Inset: voltage-saturation relation at higher resolution on the *y* axis.

(B) Saturation and equivalent pressure calculated with Equation 1 in a CL with defects.

(C) Fluorescence images of potential-induced breakthrough measured at electrolyte overpressure. The electrolyte is shown in light blue.

wetting scenario, the contact angle is assumed to be 0°, as calculated in Equation 3. For the moderate change, we use a contact angle of 54°, reported by Bienen et al. for smooth silver surfaces.[24] This results in $\tilde{V}$ = 1.5 V. Consequently, any applied potential exceeding the range of 1.5–2.2 V is unlikely to significantly advance the wetting front. Although our measurements do not fully align with this theoretical value, we observed a decrease in saturation change between potentials of 1 and 2 V. This suggests that the assumptions underlying Equation 2 adequately capture the general trends observed in the experiments.

Moreover, as illustrated in Figure 3, the magnitude of the wetting events strongly depends on the structure of the CL. In this context, "defect-free" CLs refer to those with no or only minor structural defects. By contrast, cracked CLs contain significant fractures that span a large portion of the electrode surface (see Figure S2). The effects of voltage- and pressure-induced wetting can also be additive, as demonstrated in Figure3C, when additional pressure is applied.

In defect-free CLs, the electrolyte front remains stable over time. However, a closer examination of the detailed progression of the curve (Figure 3A, inset) still shows the influence of the saturation voltage. In contrast, when defects are present, the saturated area increases significantly with applied potential. Under conditions of electrolyte overpressure, a breakthrough can even be induced. For example, when applying an initial pressure difference of 100 mbar, we observed a potential-driven breakthrough at voltages below the saturation threshold. By calculating equivalent pressures according to Equation 1 and incorporating the initial pressure difference, we obtained a value of 115 mbar, which aligns with the breakthrough pressures previously measured for multiple chips.[37] The electrolyte distribution is still influenced by the presence of smaller cracks and agglomerated catalyst particles (Figure S2). Thus, areas with slightly larger pores are wetted first and form a corridor for electrolyte breakthrough.

Notably, even low potentials, corresponding to low equivalent pressures, can cause substantial changes in saturation, particularly in CLs with defects. To mitigate the effects of electrowetting, denser CLs and the application of gas overpressure are effective strategies. Furthermore, the influence of the saturation voltage implies that at typical cell operating potentials, the additional impact of electrowetting is relatively small, suggesting that flooding primarily results from other mechanisms.

As illustrated in Figure 3, the saturation curves begin to flatten at approximately 1 V. Although this does not perfectly match the calculated value from Equation 2, the deviation is within the experimental margin of error for all measured parameters. Additionally, since no gas evolution was detected, it is reasonable to conclude that water splitting did not occur at the applied cell potentials. Once water splitting begins, the wetting front becomes chaotic as a result of gas-bubble formation.

In experiments discussed in the next section, we observed that when the electrode was supplied with a CO_2 feed and ecCO$_2$RR occurred, it often became flooded over the course of the experiment. This aligns with findings by Osiewacz et al., who demonstrated that ionic species—particularly K_2CO_3 formed during ecCO$_2$RR—significantly influence electrolyte distribution.[26] Notably, at higher potentials, the electrolyte phase boundary exhibited substantial movement. This behavior deviated from the predictions of Equation 1 and our prior measurements. Given that electrowetting was characterized without

Please cite this article in press as: Brosch et al., Visualization of CO formation at the triple-phase boundary in gas diffusion electrodes for ecCO$_2$RR, Chem (2025), https://doi.org/10.1016/j.chempr.2025.102582

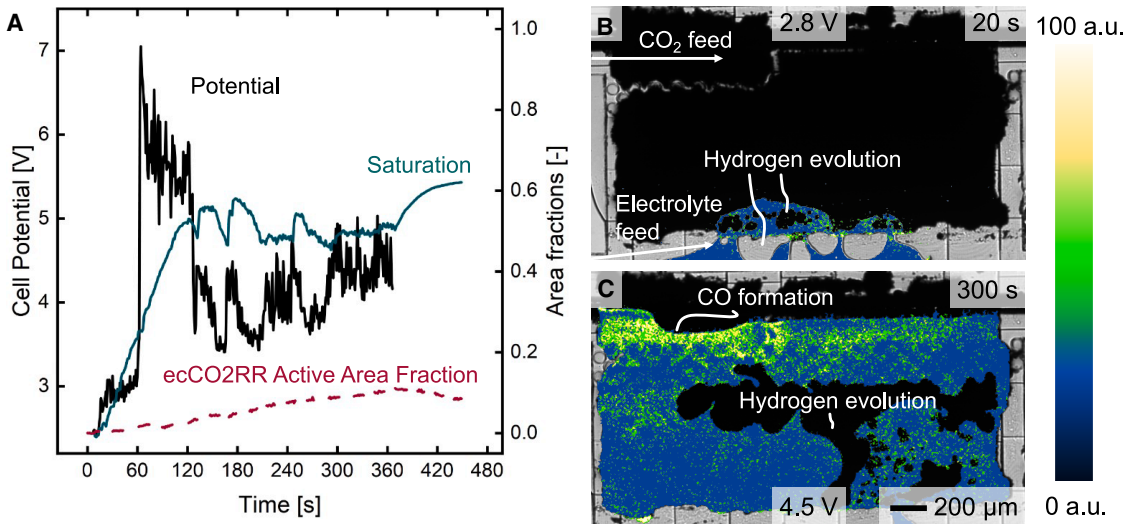

Figure 4. HER occurring in all phases of an experiment at a constant total current density of i = 10 mA cm^{-2}

(A) Potential trace at constant current density.

(B) HER at the beginning of the process before flooding at high initial potentials.

(C) HER throughout the flooded electrode under high potentials. CO_2 reduction occurs near the boundary between gas feed, solid catalyst, and electrolyte, as indicated by the green and yellow regions.

a.u. are arbitrary units of intensity scaled to the same value range for all measurements. The full experiment is shown in Video S1.

CO_2 supply, it is likely that the electrochemical reduction of CO_2 further destabilizes the phase boundary.

In conclusion, our findings highlight that in CLs with defects, even low potentials can dramatically affect electrode wettability. Conversely, in defect-free CLs, the wetting front remains comparatively stable. Additionally, controlling the pressure difference between the electrolyte and gas sides can modulate the impact of electrowetting, either inducing or preventing breakthrough. For all subsequent experiments, we equalized the pressures on the electrolyte and gas sides to primarily examine the intrinsic behavior of the electrode itself.

Spatiotemporal investigation of CO formation

To characterize general reactivity in GDEs, we previously conducted experiments using fluorescence lifetime-based tracing of local pH.[36,37] Although this method provides insights into active electrode areas, it cannot distinguish between the hydrogen evolution reaction (HER) and ecCO$_2$RR. In this study, we incorporated a CO-sensitive dye, the transition-metal complex Ru-PBP, into the electrolyte to selectively detect ecCO$_2$RR. A ligand-exchange reaction between the 2,1,3-benzothiadiazole (BTD)-ligand of the dye and CO increased fluorescence intensity. Using CLSM, we achieved spatiotemporal detection of CO within the CL of our microfluidic electrolyzer. Further details on the dye are provided in supplemental information section S4, and reference measurements validating its activity and selectivity are detailed in section S5.

Repetitions of the experimental setup produced qualitatively consistent results. However, because of the slight variations in defects across sprayed CLs in different chips, a fully quantitative comparison of measurements is not feasible.

Typical laboratory-scale operations apply a constant current density to the electrode. For ecCO$_2$RR, current densities of 100 mA cm^{-2} or higher are commonly used in cells with electrode areas ranging from 5 to 25 cm^2. However, our microfluidic cell is significantly scaled down to an electrode area of approximately 2 mm^2. This means that pressing the cell components together to improve contact is not possible, leading to significantly higher contact resistances. The cell resistance also depends heavily on the wetting degree and varies between individual chips. Resistance values range from 10 kΩ in the partially wetted state up to 38 kΩ after breakthrough. During operation, we typically measured a resistance of 12 kΩ. Additionally, contacting the CL requires wires with very small diameters, resulting in a significantly smaller contact area than that found in commercial current collectors. Consequently, we operated at reduced current densities of 10 mA cm^{-2}.

The behavior of the cell varied with the quality of the CL, including factors such as the presence of defects, the number of layers applied during the spraycoating step in the channel fabrication, and the quality of contact with the connecting wire. Observations could generally be grouped into two categories: (1) high and (2) low cell potentials.

At high cell potentials, the parasitic HER became significant. As shown in Figure 4, the HER induced the formation of gas bubbles within both the electrolyte and the CL. These gas bubbles reduced the effective catalyst area available for ecCO$_2$RR, resulting in lower saturation and less active area than experiments with lower cell potentials (see Figures 5 and S6). Furthermore, the fluctuating potential trace in Figure 4A indicates that excessive gas formation destabilized the overall process, making it considerably less stable than under conditions with minimal HER. We also observed that a fluctuation between gas formation

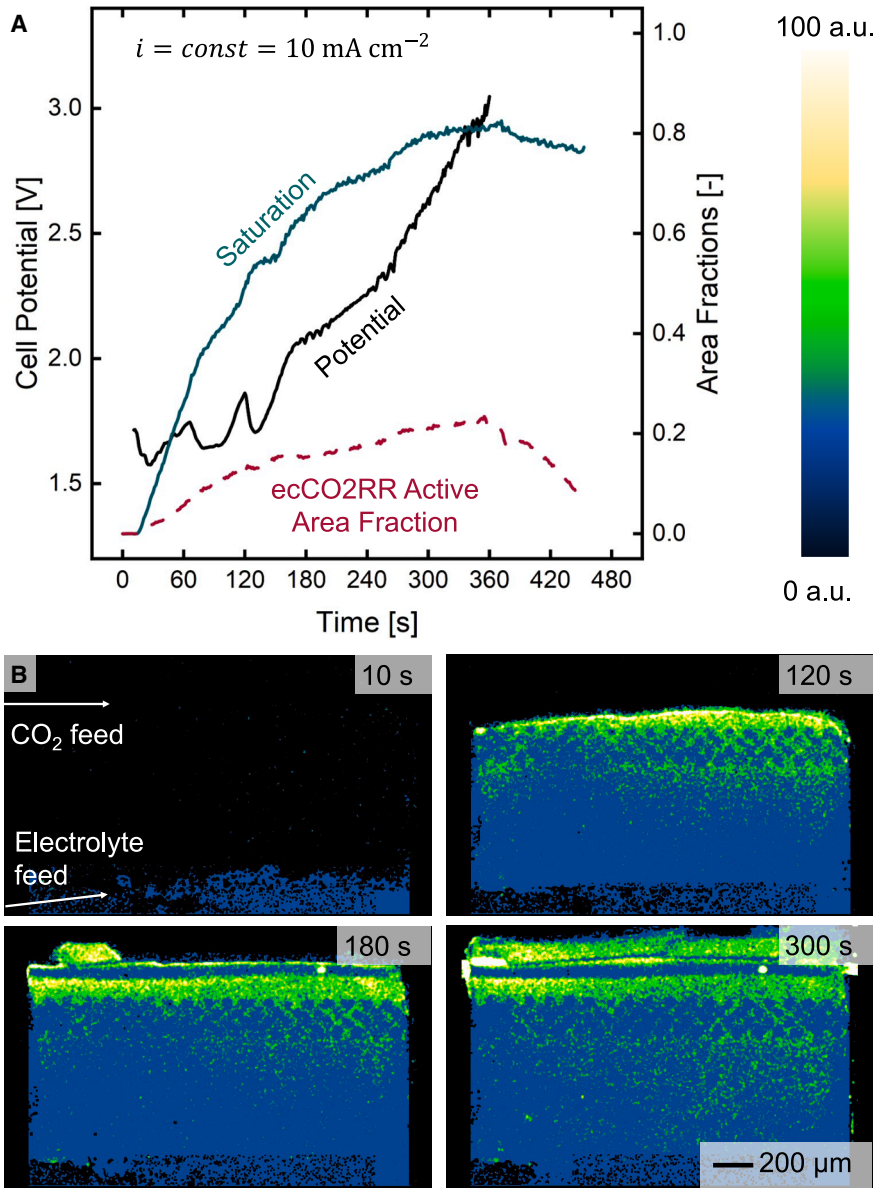

Figure 5. Experiments at a constant current density of 10 mA cm^{-2}

(A) Voltage trace and characteristic areas of the CL. Over time, the saturation reaches a value of 80%, similar to that in other experiments.

(B) CLSM images of the experiments. After 180 s, breakthrough of the electrolyte to the gas side occurs. The zone of highest reactivity was measured close to the TPB throughout the experiment.

a.u. are arbitrary units of intensity scaled to the same value range for all measurements. The full experiment is shown in Video S2.

and gas transport reflected the potential trace. To assign regions either to the presence of hydrogen or to being simply dewetted, we observed their formation over time (supplemental information section S9).

Furthermore, the highest activity for CO_2 reduction occurred near the TPB toward the CO_2 feed of the cell. The higher intensity of the Ru-PBP signal indicates a locally higher concentration of CO near the TPB. This is the first indication that CO_2 mass transport is a limiting factor in the distribution of active zones in the CL. It is not possible to assign absolute concentration values; however, a rough calibration relating the given intensity units to concentrations is given in supplemental information section S10.3.

Interestingly, the extent of electrode flooding—whether partial or complete—did not appear to significantly affect the occurrence of the HER. We observed the HER both during the onset of current, when the contact between CL and electrolyte was minimal, and in fully flooded electrodes. This suggests that saturation plays only a secondary role in determining selectivity at elevated potentials.

For comparison, Figure 5 shows a constant-current measurement at low cell potential. Initially, the electrode flooded gradually, leading to moderate fluctuations and a slow increase in cell potential. After approximately 180 s, electrolyte broke through to the gas side, after which the cell potential rose more rapidly. Electrochemical impedance spectroscopy measurements with iR compensation showed that this increase was equally caused by ohmic and charge-transfer resistances. An increase in charge-transfer resistance was expected because the reactant supply was significantly hindered upon flooding. The increase in ohmic resistance could have been due to alterations in ionic conductivity pathways as a result of interactions with the Nafion binder. Nevertheless, the zone with the highest activity toward ecCO$_2$RR was detected near the TPB. Clearly, the higher CO_2 concentration near the feed is crucial for the distribution of the reaction zones. However, a smaller amount of CO was also detected in the flooded areas of the CL. This indicates that flooding is not a significant issue as long as an active interfacial area is maintained to support reactant transport. This is further supported by measurements where we artificially fixed the location of the TPB by adjusting the feed pressures of electrolyte and CO_2. Here, we found the same behavior as without stabilization of the phase boundary (more details are given in supplemental information section S11).

In fact, recent findings suggest that cathode "weeping" in electrochemical reactors does not reduce the FE and can still support high current densities.[21] Our steady-state measurements consistently showed an electrolyte saturation of approximately 80%, aligning well with simulation results where

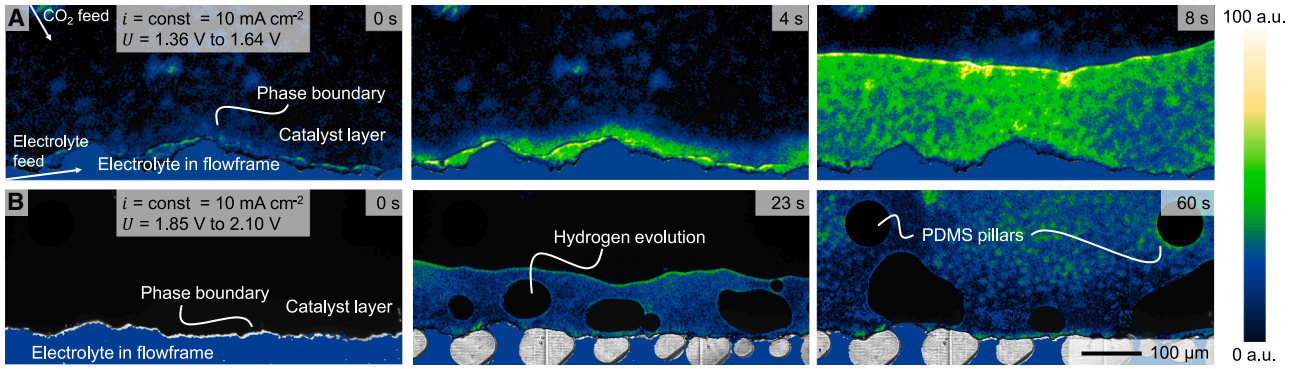

Figure 6. High-resolution imaging of the advancing phase boundary

(A) Phase boundary at first contact with the CL. The highest activity is detected at the phase boundary and in its direct vicinity.

(B) Hydrogen evolution occurs directly at first contact between the electrolyte and CL at the same current density but higher cell potential. Wetting proceeds slower than without gas-bubble formation. Lighter, non-wetted areas in the CL are defects or areas with lower particle density.

a.u. are arbitrary units of intensity scaled to the same value range for all measurements. The experiments were conducted in different channels, causing the different results. Both experiments are shown in Videos S3 and S4.

interfacial areas were found to be maximal at around 80% saturation.[53] These results emphasize that the gas-liquid interfacial area is more critical for achieving good selectivity and efficiency than preventing breakthrough or maintaining precise saturation levels. Particularly for longer measurements (see supplemental information section S10.2), we observed a constant slow transport of electrolyte to the gas side of the CL after a steady state had been established, whereas the distribution of active zones and saturation remained stable.

Two representative measurements for each case are presented here. However, the following phenomena were consistently observed across all repetitions conducted under identical conditions:

- The CL became wetted to a greater extent than predicted by the electrowetting effect (see section "electrowetting").
- The strongest Ru-PBP signal, indicative of CO formation, was detected close to the TPB.
- Hydrogen evolution occurred at elevated cell potentials (typically above 3 V) regardless of the wetting state or degree of saturation.
- Reactivity persisted throughout the wetted or flooded CL, most likely because of the CO_2 transport through non-wetted pores or the presence of dissolved CO_2.

From these experiments, we concluded that the main reaction zones are located near the TPB. However, confirming this observation would necessitate higher-resolution measurements. Additionally, the activity detected throughout the wetted electrode areas would require further investigation. To address these questions, we performed the following: (1) high-resolution scans of the phase boundary to examine it in greater detail, (2) 3D scans of the flooded electrode areas, and (3) adjustments to the amount of dissolved CO_2 in the electrolyte to evaluate the effect of dissolved reactants.

High-resolution scans of the TPB

To investigate the TPB more thoroughly, we conducted high-resolution imaging of the phase boundary during experiments at constant current density. The results for the initial contact between the electrolyte and the CL at varying potentials are shown in Figure 6. These results correspond to the two cases for the entire CL discussed in the previous section. Each experiment was conducted in a new channel with different defect structures and preparation methods, resulting in the different potentials. For lower cell potentials, the CL was applied in two steps, ensuring better contact with the cathode wire. For higher potentials, only a single, thicker layer of particles was applied, which generally led to higher contact resistances.

We made several observations regarding areas of higher reactivity and the advancement of the phase boundary. As shown in Figure 6A, the highest activity for CO production occurred directly at the electrolyte-gas phase boundary. However, some CO was also detected in the bulk electrolyte. Our measurements indicated that CO_2 mass transport significantly influenced reactivity and that CO was predominantly detected at and near the phase boundary. This was because CO_2 was supplied more efficiently through the gas feed than it could diffuse through the solution, and the CO_2 reduction reaction then proceeded significantly faster than diffusion, consuming all available CO_2. The diffusion coefficient for CO_2 was estimated as approximately 2.5×10^{-4} m^2 s^{-1} in porous media and 1×10^{-15} m^2 s^{-1} in the solution. Consequently, a high interfacial area is critical, whereas overall electrode saturation is not a sufficient indicator of performance.

In agreement with Sabharwal et al., we evaluated phase boundary areas at different saturation states (see Figure 7).[53] The results showed that the largest boundary areas were achieved at a saturation of approximately 70%. Conversely, the interfacial area was minimal when saturation was below 30% or above 80%. These findings align well with simulated results from the literature, indicating that optimal saturation for ecCO$_2$RR lies between 30% and 80%.

It should be noted that our measured values were consistently lower than the simulated ones because electrolyte or catalyst particles obscured some boundary areas within the pore network such that they were undetectable. Despite this

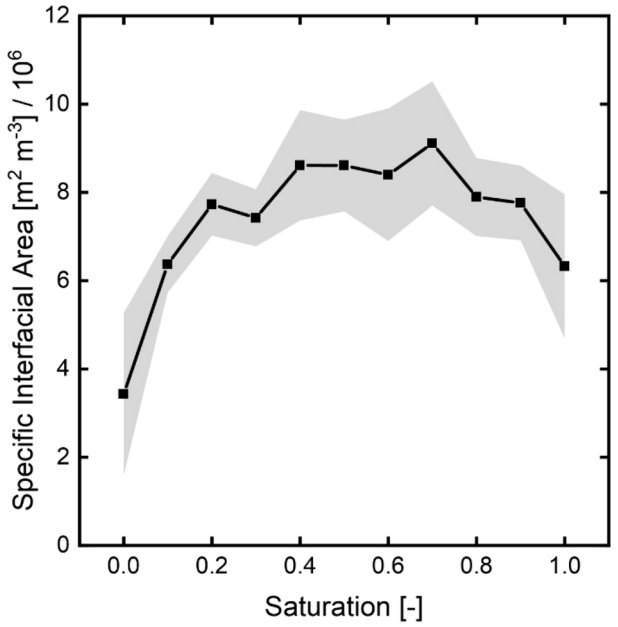

Figure 7. Specific gas-liquid interfacial area depending on saturation of the CL

The error range accounts for the standard deviation between five measurements of phase boundary lengths at each saturation level.

limitation, our experiments typically achieved saturation levels slightly below 80%, which corresponds to the range of maximum phase boundary lengths reported by Sabharwal et al.[53]

As discussed above, electrode flooding does not necessarily trigger the HER. When the cell potential remains sufficiently low, dissolved CO_2 in the flooded regions is preferentially reduced over water.

However, as shown in Figure 6B, the HER occurs immediately at higher potentials. Although the CL remains active for ecCO$_2$RR, significant amounts of hydrogen gas are formed, resulting in a lower CO yield than the low-potential case. When the contact area between CL and electrolyte increases, one of two scenarios occurs: either the potential drops, leading to a decrease in HER (as shown in Figure 5), or the potential remains high, causing HER and ecCO$_2$RR to proceed simultaneously.

3D scans of the flooded electrode areas

In most measurements, we observed that when we applied a potential or current and initiated ecCO$_2$RR, the electrolyte phase boundary advanced through the CL and eventually broke through to the current collector. Contrary to our initial assumption that reactivity occurs exclusively at the phase boundary, we detected ecCO$_2$RR activity across the entire flooded electrode area during wetting and after breakthrough. Additionally, the boundary layer thickness where CO was detected was significantly higher than expected.

Whereas the lowest mass transport and electrical resistance are expected directly at the back of the flooded electrode, the high contact area between the electrolyte and the CL appears to facilitate ecCO$_2$RR throughout the electrolyte. This suggests that dissolved CO_2 can diffuse and be reduced more readily, resulting in measurable activity across all wetted regions of the CL. Alternatively, the geometry of our channel might create localized areas of lower CO_2 resistance, particularly along the top or bottom of the channel, than the bulk of the CL.

To determine whether ecCO$_2$RR activity is confined to the geometric CL surface or distributed throughout the pore network, we performed high-resolution 3D imaging. As shown in Figure 8, we observed no variation in signal intensity across the height of the electrode. The dark line visible in the cross-sectional views in Figure 8B corresponds to the interface between the two layers of the CL, which were applied via spray coating. This region might also act as an additional pathway for enhanced CO_2 transport.

These observations suggest that dissolved CO_2 is most likely responsible for the activity measured in the bulk electrolyte. Additionally, a "spotty" texture of active areas is visible in the CLSM images. Although the grainy texture is a common artifact of the imaging method, it also indicates that the CL is not fully wetted or that the active areas are unevenly distributed. Similar behavior was reported by Rieder et al., who used X-ray diffraction (XRD) and energy-dispersive X-ray (EDX) tomography to reveal non-uniform electrolyte distribution in GDEs.[30]

Dissolved CO_2 in electrolyte

The previous measurements further confirm that CO_2 is dissolved throughout the electrolyte and can be reduced across the entire catalyst phase once direct contact between the current collector and the electrolyte is established. When a bicarbonate electrolyte is used, the equilibrium between CO_2, bicarbonate, and carbonate plays a crucial role in determining the availability of CO_2 for ecCO$_2$RR in solution:

$$CO_2 + 2H_2O \rightleftharpoons HCO_3^- + H_3O^+ \rightleftharpoons H_2CO_3 + H_2O \quad \text{(Equation 4)}$$

In the literature, mechanistic studies underline the importance of bicarbonate as a mediator for the transport of dissolved CO_2 to the catalyst surface.[54,55] Thus, a higher amount of CO_2 can be stabilized and made available for electrochemical reduction using a bicarbonate electrolyte. To validate this hypothesis, we compared measurements using nitrogen-purged electrolyte with those using CO_2-saturated electrolyte. The results are presented in Figure 9.

We observed two key differences: without dissolved CO_2, the active boundary layer is approximately half as thick as with CO_2-saturated electrolyte. Additionally, the overall signal intensity is higher with CO_2-rich electrolyte. Both findings strongly suggest that dissolved CO_2 is responsible for the CO detected in the flooded areas of the CL. Through the CO_2-bicarbonate equilibrium (Equation 4), a steady supply of dissolved CO_2 appears to be available in solution. Spectroscopic studies of ecCO$_2$RR on gold by Dunwell et al. demonstrated that this equilibrium contributes significantly to the dissolved CO_2, thereby increasing the reaction rate by enhancing the available CO_2 concentration in solution. Although ecCO$_2$RR itself increases the local pH value, which drives the bicarbonate equilibrium away from dissolved CO_2 and toward the side of bicarbonate and carbonic acid, the large CO_2 excess factor ensures a constant supply of gaseous CO_2. As described by Zhu et al., the formed bicarbonate then

Please cite this article in press as: Brosch et al., Visualization of CO formation at the triple-phase boundary in gas diffusion electrodes for ecCO$_2$RR, Chem (2025), https://doi.org/10.1016/j.chempr.2025.102582

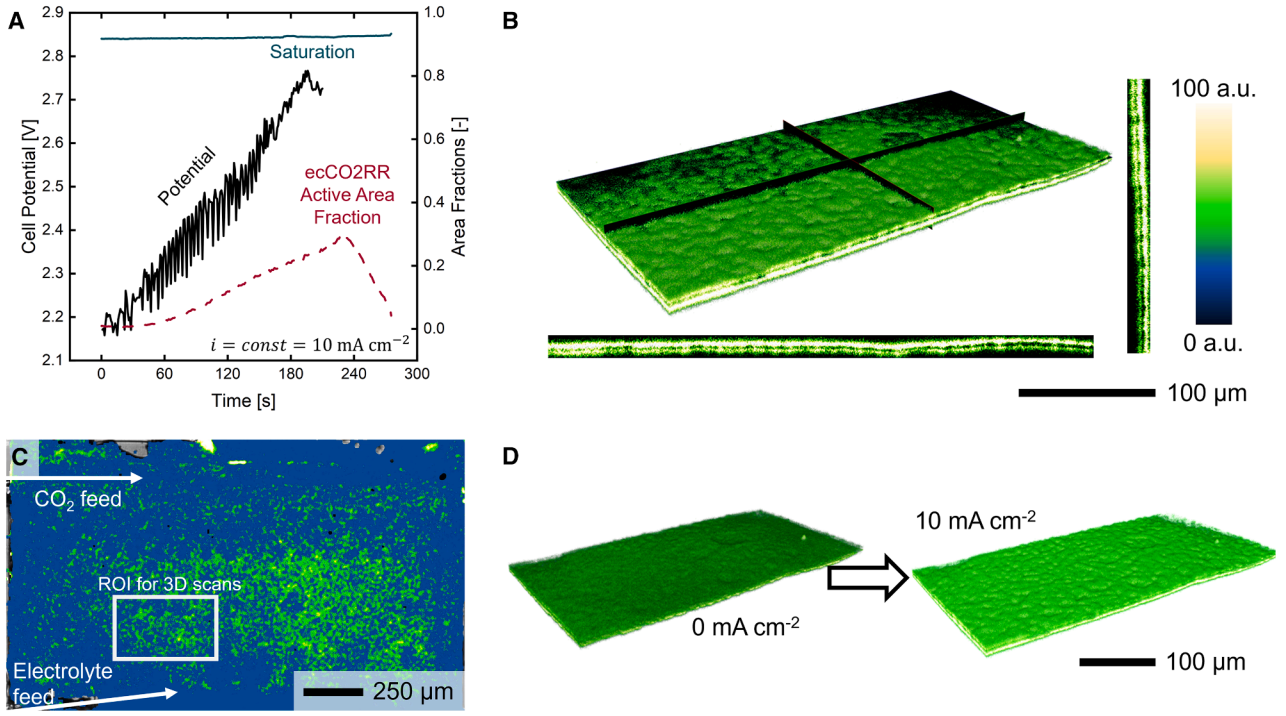

Figure 8. Operation of flooded electrode

(A) Cell potential, saturation, and CO-producing areas over time.

(B) 3D scans of flooded electrode with cross-sections showing activity throughout the entire CL. The CL was applied in a two-step coating process, which can be seen in the cross-sections.

(C) Wetting state and active areas in the flooded electrode. The highest activity occurred outside the measurement window in the gas channel (the electrolyte penetrated further into the gas channel than shown in Figure 5B, fourth panel).

(D) 3D sections of the flooded electrode before and during current flow. An increase in intensity throughout the electrode height is apparent.

a.u. are arbitrary units of intensity scaled to the same value range for all measurements.

acts as a mediator to transport freshly dissolved CO_2 to the catalyst surface.[55]

Furthermore, these results indicate that boosting CO_2 concentration—either by maximizing the interfacial area near and at the TPB or by supplying CO_2 directly to the electrolyte in addition to the gas feed—can increase overall activity. The result shown in Figure 9 indicates that under normal operating conditions, CO_2 dissolution and transport through the electrolyte are slower than the reaction. Compared with typical laboratory-scale experiments conducted at higher current densities and lower CO_2 excess, the low applied current densities and high CO_2 excess in our experiments (excess factor between 8 and 10) might exaggerate this effect of dissolved CO_2. Nonetheless, our findings demonstrate that excess CO_2 can dissolve into the electrolyte and remain reactive in other regions of the electrode.

To confirm that controlling the cell potential can reliably prevent the HER, we conducted experiments under constant-potential conditions. Our results showed that no hydrogen was formed at cell potentials below 3 V. Consequently, we selected potentials of 2 and 3 V for the constant-potential experiments. As shown in Figure 10, the results closely resemble those observed at low cell potentials during constant-current-density experiments, as discussed above.

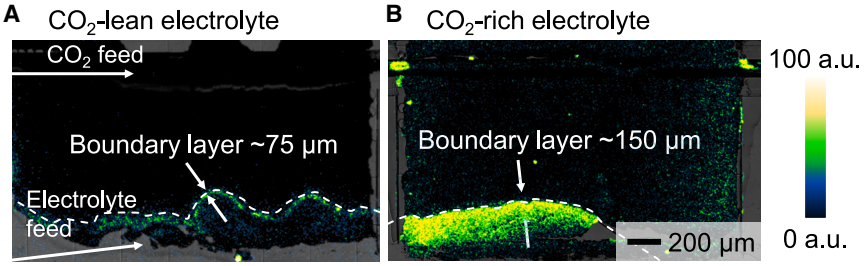

Figure 9. Comparison between measurements

(A) Nitrogen-purged electrolyte.

(B) CO_2-saturated electrolyte.

a.u. are arbitrary units of intensity scaled to the same value range for all measurements. We removed all values below 50 a.u. to increase the visibility of the active boundary area. Dashed lines indicate the electrolyte phase boundary.

Please cite this article in press as: Brosch et al., Visualization of CO formation at the triple-phase boundary in gas diffusion electrodes for $ecCO_2RR$, Chem (2025), https://doi.org/10.1016/j.chempr.2025.102582

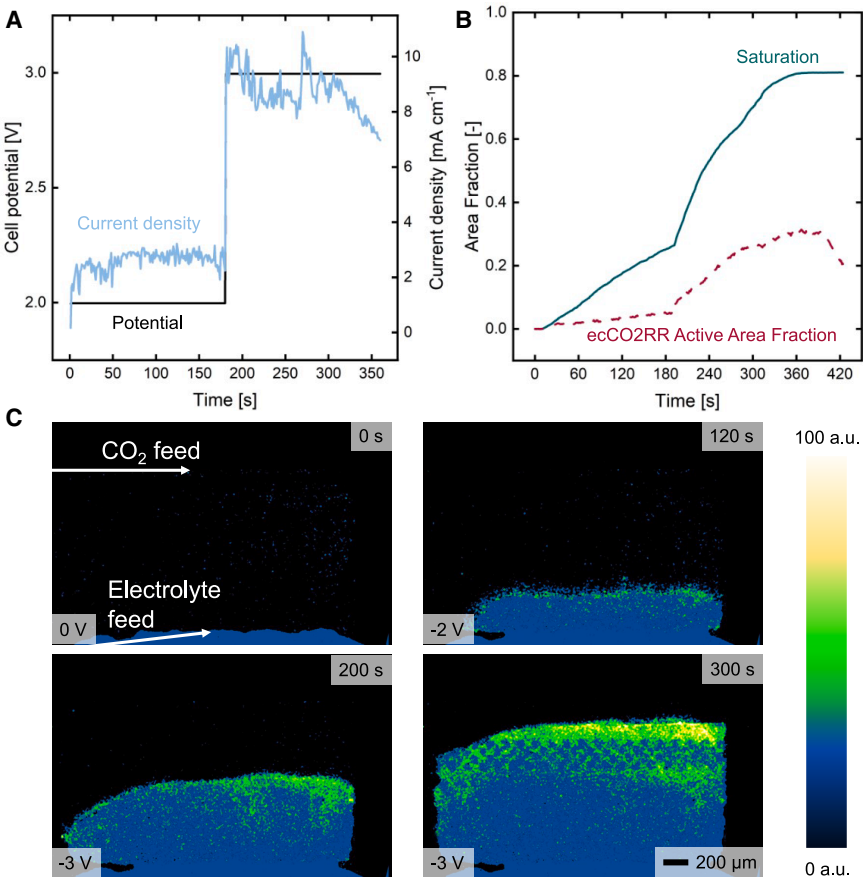

Figure 10. Constant-potential experiment

(A) Current and voltage trace for both applied cell potentials.

(B) Saturation and active area for $ecCO_2RR$. The saturation increases to a new steady state defined by potential and reaction.

(C) CLSM images of different stages of the experiment. 0 s: the onset of potential induces wetting. 120 s: partial wetting of the CL occurs, and a thin active boundary layer develops. 200 s: the increase in voltage increases the active area and saturated area. 300 s: saturation reaches a steady state at 80%, CO_2 dissolves into the electrolyte, and the fraction of active area increases.

a.u. are arbitrary units of intensity scaled to the same value range for all measurements. The full experiment is shown in Video S5.

Current, saturation, and the fraction of active area closely follow the applied cell potential. At 2 V, the current density stabilized at 2 mA cm^{-2}. As the cell potential increased, the current density rose proportionally. However, after approximately 300 s, the current density began to decline. This behavior is typical in constant-potential experiments and suggests that reactant depletion occurs because mass transport cannot keep pace with the reaction rate.

CLSM images in Figure 10C provide local resolution of activity. The highest activity was consistently observed near the TPB. At most, 35% of the wetted area exhibited activity for $ecCO_2RR$, and the most significant activity was always located close to the phase boundary. The fraction of active area increased as the cell potential rose until mass-transport limitations became dominant at 300 s. Beyond this point, the current density decreased, and the fraction of active area stagnated.

Overall, these experiments support our previous hypotheses and findings by reinforcing the critical role of mass transport and the phase boundary in determining $ecCO_2RR$ activity.

DISCUSSION

In this work, we investigated electrowetting in detail as a critical factor influencing electrode wettability. We observed that increasing the cell potential raised the saturation level, which reached up to 60% depending on the defect structure of the CL. However, under experimental conditions, the saturation often exceeded this value (at approximately 80%) and frequently broke through to the gas side. Notably, we could reproduce breakthrough without $ecCO_2RR$ only by applying an additional pressure across the electrode. These findings suggest that ionic species formed or precipitated during $ecCO_2RR$ significantly influence wetting behavior and thus render the electrode more hydrophilic than anticipated by electrowetting alone. This conclusion aligns with reports in the literature, where salt deposition and reaction-induced breakthrough were observed in both experiments and simulations.[21,24,26,28,30,35]

Our results consistently showed the highest CO concentrations in the CL areas at the TPB regardless of the saturation state. Although CLSM does not have a sufficiently high resolution to visualize reaction sites on a molecular level, we can still clearly show the distribution of reactive zones throughout the CL *in operando*. This highlights the importance of a larger interfacial area (or TPB area) in enhancing electrode efficiency. We found that the TPB area observed for various saturation levels in our experiments closely matched simulated predictions from the literature.[53]

Using the presented dye system, we differentiated CL areas producing CO from those producing hydrogen. We demonstrated that the HER could occur throughout the CL regardless of the wetting state. In steady-state conditions, the HER primarily occurs in the flooded electrode, whereas it is suppressed at the TPB by the high CO_2 concentration. However, electrode flooding only partly explains the HER. In experiments with flooded CLs, no significant hydrogen formation was detected under appropriate conditions. These findings confirm that controlling the cell potential (and consequently the electrode potential) is crucial in defining selectivity. Given that the HER was also detected in

electrodes with 0% electrolyte saturation, it is evident that only maintaining low cell potentials can prevent hydrogen formation.

If the cell potential is kept low (in our cell, the HER typically occurred above 3 V), CO can also form in the bulk electrolyte, although the CO concentration consistently remains higher at the TPB. We measured the thickness of the boundary layer where CO had formed for both CO_2-rich and CO_2-lean electrolytes. Dissolved CO_2 in the electrolyte increased the width of this boundary layer. As long as sufficient CO_2 is transported into the electrolyte, this suggests that the entire thickness of the CL could be active for ecCO$_2$RR. Typical CL thicknesses in laboratory-scale electrolyzers range from 5 to 50 μm, whereas the boundary-layer thickness measured in our experiments exceeded this range.

We repeated constant-current experiments with CLs of varying thicknesses and observed that the boundary-layer thickness remained approximately constant. Additionally, we investigated the impact of different current densities. At lower current densities, the boundary layer was less pronounced, suggesting that at laboratory-scale or industrially relevant current densities, the boundary layer might be thinner than what we measured in this study. When measuring only the layer with the highest CO concentration at the TPB, we obtained values from 8 and 10 μm, likely providing a more accurate estimate of the active boundary-layer thickness under practical conditions.

However, compared with a typical electrode, our microfluidic electrolyzer has an inverse aspect ratio. This configuration can enable gas transport along the top and bottom of the electrode, where porosity is higher (comparable to the dimensions of a crack or defect in the CL) than in the bulk CL. This increased porosity most likely enhances gas transport, thereby increasing the volume accessible for fast gas transport and extending the boundary-layer thickness. Consequently, it is not possible to provide a definitive quantitative value for the layer thickness solely on the basis of our measurements.

Limitations

Some characteristics of the presented method limit its applicability to certain channel geometries and process conditions. Because CLSM is an optical method, the penetration depth into the CL is limited, and areas containing larger agglomerates cannot be accurately depicted. Additionally, the flow rate of the electrolyte needs to be high enough for the fluorescent dye to be constantly removed and refreshed so constant conditions can be ensured. Other points of concern could be the stability of Ru-PBP under reaction conditions, the long-term stability, or the possible calibration of the system. A more thorough discussion of the potential limitations of this method can be found in supplemental information section S10. However, the findings presented in this work are not affected by these limitations, and this discussion is mainly given to indicate the method's applicability to other systems.

Conclusions

In this work, we studied the impact of potential-driven electrowetting in isolation from electrochemical reactions. Additionally, we conducted a series of electrochemical experiments to examine the phenomena occurring at the TPB between the liquid electrolyte, solid CL, and gaseous reactant feed. On the basis of these experiments, we draw the following conclusions for silver-based CLs with Nafion binders and bicarbonate electrolytes:

- Potential-driven electrowetting alone does not account for electrode flooding; salt precipitation most likely has an additional influence.
- The highest activity for ecCO$_2$RR is measured in the CL regions closest to the TPB.
- The interfacial area is generally highest for saturation between 30% and 80%.
- The HER can occur throughout the CL depending on the cell potential.
- In flooded regions, CO formation can be detected throughout the entire height of the CL.
- Dissolved CO_2 from the bulk electrolyte is reduced to CO as well. Thus, the TPB is crucial for fast mass transport but is not essential for ecCO$_2$RR to occur.
- The active boundary-layer thickness depends on the current density and CO_2 excess and can include the entire thickness of the CL.

Our results align well with observations reported by other groups about interfacial areas, presumed reaction sites, voltage-saturation relationships, and other factors influencing electrode efficiency. Importantly, we have demonstrated the ability to localize active areas within the CLs of GDEs *in operando*, significantly enhancing our understanding of reaction processes at multiphase boundaries.

The tools and findings presented in this work enable a more targeted approach to designing CLs for GDEs, allowing for optimization tailored to specific processes. This improved understanding can also contribute to reducing the use of scarce precious metals, promoting more sustainable and efficient electrode designs.

METHODS

Fabrication of microfluidic chips

Microfluidic master structures were designed in Autodesk Inventor 2023 and printed on a Nanoscribe Photonic Professional GT+ two-photon polymerization 3D printer using IP-S resin (Nanoscribe). The printed part was washed with propylene glycol monomethyl ether acetate (PEGMEA) for 10 min to remove residual resin. The negatives were cast in polydimethylsiloxane (PDMS; SYLGARD 184 Silicone Elastomer Kit mixed in a ratio of 1:10 catalyst/elastomer base), degassed in a vacuum desiccator for 1 h, and cured at 55°C for at least 4 h. Afterward, the channels were cut from the PDMS blocks, the inlets and outlets for tubing and wires were punched with 1.2 mm biopsy punches, and the channels were cleaned in isopropanol. Silver wire with a diameter of 50 μm was inserted into the designated channels (Figure S7) and glued in place in the punched holes with UHU Max Repair Power glue. We prepared a catalyst ink consisting of 100 mg of silver nanoparticles (particle size 50–60 nm), 200 μL Nafion NS-5 solution, and 2 mL isopropanol by mixing and sonicating the ingredients. Directly after sonication, the ink was spraycoated with an airbrush pistol (nozzle width 0.2 mm)

onto the masked and preheated (120°C) channels. One batch of catalyst ink was sufficient for six channels. After spraycoating, the channels were sintered in a vacuum oven at 130°C for 3 h. Afterward, the channels were plasmabonded to PDMS-coated microscopy slides in an oxygen plasma oven (Diener Zepto) (60 W, 42 s, 0.4 mbar).

Synthesis of CO-detecting complex

The CO-detecting ruthenium complex ([Ru(CH=CHPyr-1)Cl(CO)(BTD)(PPh_3)$_2$]) was synthesized according to the published procedure.[50] A solution of 25 mg BTD and 101.8 mg [RuHCl(CO)(PPh_3)$_3$] in 10 mL dichloromethane (DCM) was prepared and stirred at room temperature for 30 min. Then, 36.5 mg of 1-ethynylpyrene was added, and the mixture was stirred at room temperature for 1 h. 25 mL methanol was added, and the mixture was chilled at −20°C for 2 h. The precipitated orange crystals were filtered and dried in a vacuum. Yield: 71%. ^{1}H NMR (400 MHz, $CDCl_3$) δ 8.39–7.85 (m, 12H), 7.84–7.71 (m, 2H), 7.69–7.01 (m, 30H), 7.00–6.98 (m, 1H) ppm).

Reference measurements with CORM-3, hydrogen, and CO_2

0.1 mmol L^{-1} complex dye was dissolved in electrolyte (0.5 mol L^{-1} $KHCO_3$ in 10:1 [vol] water/DMSO). For reference measurements, samples of 2 mL each were prepared. 2 mg tricarbonylchloro-(glycinato)-ruthenium (II) (CO-releasing molecule 3 [CORM-3]) were added to one sample, and the other two were each stored for 5 min in a pressure chamber with 2 bar overpressure of H_2 or CO_2. Afterward, the respective gases were carefully bubbled through the sample for 10 s, ensuring good contact between the dye and test substance. The samples and an untreated reference sample were filled into an empty microfluidic channel, and the fluorescence intensity was measured at the same settings and locations in the channel for each sample. The mean gray values were extracted with ImageJ. The measurements were done for empty channels and catalyst-filled channels.

Electrowetting measurements

For electrowetting measurements, the channel was filled with electrolyte, and on the gas side, air was supplied for counter pressure. Potentials were applied with a Gamry Reference 3000 potentiostat using a two-electrode setup. Potentials were set for the entire duration of the experiment against the internal reference of the potentiostat. The small scale of the channels prevented an external reference electrode from being implemented. Depending on the particular experiment, differential pressures between 0 and 100 mbar were applied. A potential was set, held until steady state was reached, and increased in steps of 250 or 500 mV. Potential-driven experiments were performed with the CO-sensing complex dye, and its residual fluorescence at strong excitation intensity in the inactive state was sufficient for detecting the electrolyte phase.

Electrolysis experiments

In a typical experiment, a microfluidic chip was placed on a Leica TCS SP8 FALCON confocal microscope, the electrode wires were connected, and the chip was connected to the electrolyte and gas feed in a parallel flow-by configuration. The flowframe of the chip was carefully filled with electrolyte, and equal gas and electrolyte pressures were set. The phase boundary of the electrolyte was maneuvered toward the lower edge of the CL, ensuring electrical contact. For electrolysis experiments, constant potential or constant current density was applied for 6 min. Fluorescence images were recorded before a potential was applied and for some time after the potential had been switched off again. In all electrolysis experiments, the dye Texas Red was used for measuring saturation, and the CO-detecting complex was used for measuring activity. Both dyes were measured simultaneously via sequential scanning with different excitation and emission wavelengths (see section "imaging conditions").

Imaging conditions

For electrowetting measurements, an excitation wavelength of 405 nm and detection range of 417–558 nm were set. For all other measurements in a second measurement channel, Texas Red was measured with an excitation wavelength of 570 nm and a detection range of 612–750 nm. Measurements of Texas Red were conducted inversely: the fluorescence emission of Texas Red was quenched completely by the CO-sensitive dye. However, at the set wavelengths for the Texas Red channel, the microfluidic channel reflected the light. This reflected light was absorbed by Texas Red, resulting in areas where no fluorescence could be measured in the Texas Red channel. These corresponded to saturated areas. An HC PL FLUOTAR 4×/0.13 objective was used for imaging the entire CL. The lateral resolution was 2.827 μm px^{-1} with a depth of field of approximately 30 μm. For high-resolution images and 3D stacks, an HC PL APO 20×/0.75 CS2 objective was used. The lateral resolution was 0.571 μm px^{-1} with a depth of field of approximately 1 μm.

Image evaluation

Image segmentation was done for quantitative evaluation of the measured fluorescence images. The areas were determined in MATLAB R2020b, and lookup tables were applied in Fiji version 2.9.0/1.53t. All thresholds were set as a weighted percentage of the intensity histogram of each image. To obtain the saturation, we inverted the images from the Texas Red channel and applied an intensity threshold. The threshold was determined for each series at 20% of the histogram. We summed the remaining areas and determined the relative saturation by dividing by the area of the CL. To obtain activity, we set the threshold to 95% of the histogram. We summed the remaining areas and divided them by the area of the CL to obtain the active area. For all evaluations, non-moving artifacts (such as small dust particles) were subtracted from the images. For visualization purposes only, we applied a lookup table to depict different levels of activity. We smoothed saturation images to allow for easy differentiation between saturation and activity information.

RESOURCE AVAILABILITY

Lead contact

Requests for further information and resources should be directed to and will be fulfilled by the lead contact, Sebastian Brosch (sebastian.brosch@rwth-aachen.de).

Materials availability

This study did not generate new materials.

Data and code availability

- All data reported in this paper will be shared by the lead contact upon request.
- All original code is available from the lead contact upon request.
- Any additional information required for reanalyzing the data reported in this paper is available from the lead contact upon request.

ACKNOWLEDGMENTS

M.W. acknowledges DFG funding through Gottfried Wilhelm Leibniz Award 2019 (WE 4678/12-1). M.W. also acknowledges support from an Alexander-von-Humboldt Professorship and the European Research Council under the European Union's Horizon 2020 Research and Innovation Programme (grant agreement no. 694946). The authors thank all members of the lab for their support.

AUTHOR CONTRIBUTIONS

Conceptualization, S.B., W.P., and M.W.; methodology, S.B., E.H., O.F., and W.P.; validation, S.B. and W.P.; formal analysis, S.B., E.H., O.F., and P.S.; investigation, S.B., E.H., O.F., and P.S.; data curation, S.B., E.H., O.F., and P.S.; writing – original draft, S.B.; writing – review & editing, S.B., E.H., O.F., P.S., W.P., and M.W.; visualization, S.B.; supervision, M.W.; project administration, M.W.; funding acquisition, M.W.

DECLARATION OF INTERESTS

The authors declare no competing interests.

DECLARATION OF GENERATIVE AI AND AI-ASSISTED TECHNOLOGIES IN THE WRITING PROCESS

During the preparation of this work, the authors used Writefull in order to improve the language and readability of the manuscript. After using this tool, the authors reviewed and edited the content as needed and take full responsibility for the content of the publication.

SUPPLEMENTAL INFORMATION

Supplemental information can be found online at https://doi.org/10.1016/j.chempr.2025.102582.

Received: January 31, 2025
Revised: March 19, 2025
Accepted: April 15, 2025
Published: May 9, 2025

REFERENCES

1. Rabiee, H., Ge, L., Zhang, X., Hu, S., Li, M., and Yuan, Z. (2021). Gas diffusion electrodes (GDEs) for electrochemical reduction of carbon dioxide, carbon monoxide, and dinitrogen to value-added products: a review. Energy Environ. Sci. *14*, 1959–2008. https://doi.org/10.1039/D0EE03756G.
2. Lee, M.Y., Park, K.T., Lee, W., Lim, H., Kwon, Y., and Kang, S. (2020). Current achievements and the future direction of electrochemical CO_2 reduction: a short review. Crit. Rev. Environ. Sci. Technol. *50*, 769–815. https://doi.org/10.1080/10643389.2019.1631991.
3. Jones, J.P., Prakash, G.K.S., and Olah, G.A. (2014). Electrochemical CO_2 reduction: recent advances and current trends. Isr. J. Chem. *54*, 1451–1466. https://doi.org/10.1002/ijch.201400081.
4. Baitalow, K., Köller, N., Bacmeister, P., Keller, R., and Wessling, M. (2023). On the operation of switchable oxygen depolarized cathodes. Chem. Eng. J. *469*, 143759. https://doi.org/10.1016/j.cej.2023.143759.
5. Hernandez-Aldave, S., and Andreoli, E. (2022). Oxygen depolarised cathode as a learning platform for CO_2 gas diffusion electrodes. Catal. Sci. Technol. *12*, 3412–3420. https://doi.org/10.1039/D2CY00443G.
6. Zhou, Y., Wang, K., Zheng, S., Cheng, X., He, Y., Qin, W., Zhang, X., Chang, H., Zhong, N., and He, X. (2024). Advancements in electrochemical CO_2 reduction reaction: a review on CO_2 mass transport enhancement strategies. Chem. Eng. J. *486*, 150169. https://doi.org/10.1016/j.cej.2024.150169.
7. Nguyen, T.N., and Dinh, C.T. (2020). Gas diffusion electrode design for electrochemical carbon dioxide reduction. Chem. Soc. Rev. *49*, 7488–7504. https://doi.org/10.1039/D0CS00230E.
8. Möller, T., Ngo Thanh, T., Wang, X., Ju, W., Jovanov, Z., and Strasser, P. (2021). The product selectivity zones in gas diffusion electrodes during the electrocatalytic reduction of CO_2. Energy Environ. Sci. *14*, 5995–6006. https://doi.org/10.1039/D1EE01696B.
9. Tan, Y.C., Lee, K.B., Song, H., and Oh, J. (2020). Modulating local CO_2 concentration as a general strategy for enhancing C–C coupling in CO_2 electroreduction. Joule *4*, 1104–1120. https://doi.org/10.1016/j.joule.2020.03.013.
10. Zhang, L., Wang, Z., Mehio, N., Jin, X., and Dai, S. (2016). Thickness- and particle-size-dependent electrochemical reduction of carbon dioxide on thin-layer porous silver electrodes. ChemSusChem *9*, 428–432. https://doi.org/10.1002/cssc.201501637.
11. Nesbitt, N.T., Burdyny, T., Simonson, H., Salvatore, D., Bohra, D., Kas, R., and Smith, W.A. (2020). Liquid-solid boundaries dominate activity of CO_2 reduction on gas-diffusion electrodes. ACS Cat. *10*, 14093–14106. https://doi.org/10.1021/acscatal.0c03319.
12. Leonard, M.E., Clarke, L.E., Forner-Cuenca, A., Brown, S.M., and Brushett, F.R. (2020). Investigating electrode flooding in a flowing electrolyte, gas-fed carbon dioxide electrolyzer. ChemSusChem *13*, 400–411. https://doi.org/10.1002/cssc.201902547.
13. Yano, H., Shirai, F., Nakayama, M., and Ogura, K. (2002). Electrochemical reduction of CO_2 at three-phase (gas|liquid|solid) and two-phase (liquid|solid) interfaces on Ag electrodes. J. Electroanal. Chem. *533*, 113–118. https://doi.org/10.1016/S0022-0728(02)01078-1.
14. Li, J., Chen, G., Zhu, Y., Liang, Z., Pei, A., Wu, C.L., Wang, H., Lee, H.R., Liu, K., Chu, S., et al. (2018). Efficient electrocatalytic CO_2 reduction on a three-phase interface. Nat. Catal. *1*, 592–600. https://doi.org/10.1038/s41929-018-0108-3.
15. Xing, Z., Hu, L., Ripatti, D.S., Hu, X., and Feng, X. (2021). Enhancing carbon dioxide gas-diffusion electrolysis by creating a hydrophobic catalyst microenvironment. Nat. Commun. *12*, 136. https://doi.org/10.1038/s41467-020-20397-5.
16. Bernasconi, F., Senocrate, A., Kraus, P., and Battaglia, C. (2023). Enhancing C $\geq$ 2 product selectivity in electrochemical CO_2 reduction by controlling the microstructure of gas diffusion electrodes. EES Catal. *1*, 1009–1016. https://doi.org/10.1039/D3EY00140G.
17. Moore, T., Xia, X., Baker, S.E., Duoss, E.B., and Beck, V.A. (2021). Elucidating mass transport regimes in gas diffusion electrodes for CO_2 electroreduction. ACS Energy Lett. *6*, 3600–3606. https://doi.org/10.1021/acsenergylett.1c01513.
18. Junge Puring, K., Siegmund, D., Timm, J., Möllenbruck, F., Schemme, S., Marschall, R., and Apfel, U.P. (2021). Electrochemical CO_2 reduction: tailoring catalyst layers in gas diffusion electrodes. Adv. Sustain. Syst. *5*, 1–13. https://doi.org/10.1002/adsu.202000088.
19. Vennekoetter, J.B., Sengpiel, R., and Wessling, M. (2019). Beyond the catalyst: how electrode and reactor design determine the product spectrum during electrochemical CO_2 reduction. Chem. Eng. J. *364*, 89–101. https://doi.org/10.1016/j.cej.2019.01.045.
20. Reyes, A., Jansonius, R.P., Mowbray, B.A.W., Cao, Y., Wheeler, D.G., Chau, J., Dvorak, D.J., and Berlinguette, C.P. (2020). Managing hydration at the cathode enables efficient CO_2 electrolysis at commercially relevant

current densities. ACS Energy Lett. *5*, 1612–1618. https://doi.org/10.1021/acsenergylett.0c00637.

21. Wrobel, M., Kriescher, S., Schiffer, T., Keller, R., and Wessling, M. (2023). On the weeping of the GDE cathode during bipolar membrane-based electrochemical CO_2 reduction reaction at high current densities. Chem. Eng. J. *474*, 145335. https://doi.org/10.1016/j.cej.2023.145335.
22. Lorenzutti, F., and Haussener, S. (2023). Morphology and transport characterization of catalyst layers for CO_2 reduction. J. Electrochem. Soc. *170*, 104507. https://doi.org/10.1149/1945-7111/acff1c.
23. Kunz, P., Paulisch, M., Osenberg, M., Bischof, B., Manke, I., and Nieken, U. (2020). Prediction of electrolyte distribution in technical gas diffusion electrodes: from imaging to SPH simulations. Transp. Porous Media *132*, 381–403. https://doi.org/10.1007/s11242-020-01396-y.
24. Bienen, F., Paulisch, M.C., Mager, T., Osiewacz, J., Nazari, M., Osenberg, M., Ellendorff, B., Turek, T., Nieken, U., Manke, I., et al. (2023). Investigating the electrowetting of silver-based gas-diffusion electrodes during oxygen reduction reaction with electrochemical and optical methods. Electrochemical Science Adv. *3*, e2100158. https://doi.org/10.1002/elsa.202100158.
25. Mugele, F., and Baret, J.C. (2005). Electrowetting: from basics to applications. J. Phys.: Condens. Matter *17*, R705–R774. https://doi.org/10.1088/0953-8984/17/28/R01.
26. Osiewacz, J., Löffelholz, M., Ellendorff, B., and Turek, T. (2024). Modeling mass transfer limitations driven by electrowetting in electrochemical CO_2 reduction at silver gas diffusion electrodes. J. Power Sources *603*, 234430. https://doi.org/10.1016/j.jpowsour.2024.234430.
27. Paulisch, M.C., Gebhard, M., Franzen, D., Hilger, A., Osenberg, M., Kardjilov, N., Ellendorff, B., Turek, T., Roth, C., and Manke, I. (2019). Operando laboratory X-ray imaging of silver-based gas diffusion electrodes during oxygen reduction reaction in highly alkaline media. Materials *12*, 2686. https://doi.org/10.3390/ma12172686.
28. Paulisch, M.C., Gebhard, M., Franzen, D., Hilger, A., Osenberg, M., Marathe, S., Rau, C., Ellendorff, B., Turek, T., Roth, C., et al. (2021). Operando synchrotron imaging of electrolyte distribution in silver-based gas diffusion electrodes during oxygen reduction reaction in highly alkaline media. ACS Appl. Energy Mater. *4*, 7497–7503. https://doi.org/10.1021/acsaem.1c01524.
29. Kim, J., Lee, S.Y., Kim, S.J., Koo, B., Chung, J., Lee, D., Choi, S., Kim, J., Seo, S., Nam, C., et al. (2024). Spatiotemporal active phase evolution for CO_2 electrocatalysis. Joule *8*, 3373–3385. https://doi.org/10.1016/j.joule.2024.09.008.
30. Rieder, A., Lorenzetti, J., Zelocualtecatl Montiel, I., Dutta, A., Iarchuk, A., Mirolo, M., Drnec, J., Lorenzutti, F., Haussener, S., Kovács, N., et al. (2024). ICP–MS assisted EDX tomography: a robust method for studying electrolyte penetration phenomena in gas diffusion electrodes applied to CO_2 electrolysis. Small Methods *8*, e2400200. https://doi.org/10.1002/smtd.202400200.
31. Lu, X., Zhou, C., Delima, R.S., Lees, E.W., Soni, A., Dvorak, D.J., Ren, S., Ji, T., Bahi, A., Ko, F., et al. (2024). Visualization of CO_2 electrolysis using optical coherence tomography. Nat. Chem. *16*, 979–987. https://doi.org/10.1038/s41557-024-01465-5.
32. Yu, M., Sui, P.F., Tang, Y.F., Zhang, T., Liu, S., Fu, X.Z., Luo, J.L., and Liu, S. (2024). Visualizing electrochemical CO_2 conversion via the emerging scanning electrochemical microscope: fundamentals, applications and perspectives. Small Methods *8*, e2301778. https://doi.org/10.1002/smtd.202301778.
33. Schatz, M., Kochs, J.F., Jovanovic, S., Eichel, R.A., and Granwehr, J. (2023). Interplay of local pH and cation hydrolysis during electrochemical CO_2 reduction visualized by in operando chemical shift-resolved magnetic resonance imaging. J. Phys. Chem. C *127*, 18986–18996. https://doi.org/10.1021/acs.jpcc.3c03563.
34. Böhme, A., Bui, J.C., Fenwick, A.Q., Bhide, R., Feltenberger, C.N., Welch, A.J., King, A.J., Bell, A.T., Weber, A.Z., Ardo, S., et al. (2023). Direct observation of the local microenvironment in inhomogeneous CO_2 reduction gas diffusion electrodes via versatile pOH imaging. Energy Environ. Sci. *16*, 1783–1795. https://doi.org/10.1039/D2EE02607D.
35. Graf, A.M., Cochard, T., Amini, K., Emanuel, M.S., Rubinstein, S.M., and Aziz, M.J. (2024). Quantitative local state of charge mapping by operando electrochemical fluorescence microscopy in porous electrodes. Energy Adv. *3*, 2468–2478. https://doi.org/10.1039/D4YA00362D.
36. Kalde, A.M., Grosseheide, M., Brosch, S., Pape, S.V., Keller, R.G., Linkhorst, J., and Wessling, M. (2022). Micromodel of a gas diffusion electrode tracks in-operando pore-scale wetting phenomena. Small *18*, e2204012. https://doi.org/10.1002/smll.202204012.
37. Brosch, S., Wiesner, F., Decker, A., Linkhorst, J., and Wessling, M. (2024). Spatio-temporal electrowetting and reaction monitoring in microfluidic gas diffusion electrode elucidates mass transport limitations. Small *20*, e2310427. https://doi.org/10.1002/smll.202310427.
38. Alberts, B., Johnson, A., Lewis, J., Raff, M., Roberts, K., and Walter, P. (2002). Visualizing molecules in living cells. In Molecular Biology of the Cell, Fourth Edition (Garland Science), pp. 1474–1501. https://www.ncbi.nlm.nih.gov/books/NBK26893/.
39. Cho, S.H., Suh, J.M., Eom, T.H., Kim, T., and Jang, H.W. (2021). Colorimetric sensors for toxic and hazardous gas detection: a review. Electron. Mater. Lett. *17*, 1–17. https://doi.org/10.1007/s13391-020-00254-9.
40. Mukhopadhyay, S., Sarkar, A., Chattopadhyay, P., and Dhara, K. (2020). Recent advances in fluorescence light-up endogenous and exogenous carbon monoxide detection in biology. Chem. Asian J. *15*, 3162–3179. https://doi.org/10.1002/asia.202000892.
41. Xie, C., Luo, K., Tan, L., Yang, Q., Zhao, X., and Zhou, L. (2022). A review for in vitro and in vivo detection and imaging of gaseous signal molecule carbon monoxide by fluorescent probes. Molecules *27*, 8842. https://doi.org/10.3390/molecules27248842.
42. Pal, S., Mukherjee, M., Sen, B., Mandal, S.K., Lohar, S., Chattopadhyay, P., and Dhara, K. (2015). A new fluorogenic probe for the selective detection of carbon monoxide in aqueous medium based on Pd(0) mediated reaction. Chem. Commun. *51*, 4410–4413. https://doi.org/10.1039/C5CC00902B.
43. Feng, W., Liu, D., Feng, S., and Feng, G. (2016). Readily available fluorescent probe for carbon monoxide imaging in living cells. Anal. Chem. *88*, 10648–10653. https://doi.org/10.1021/acs.analchem.6b03073.
44. Feng, W., Liu, D., Zhai, Q., and Feng, G. (2017). Lighting up carbon monoxide in living cells by a readily available and highly sensitive colorimetric and fluorescent probe. Sens. Actuators B *240*, 625–630. https://doi.org/10.1016/j.snb.2016.09.023.
45. Feng, S., Liu, D., Feng, W., and Feng, G. (2017). Allyl fluorescein ethers as promising fluorescent probes for carbon monoxide imaging in living cells. Anal. Chem. *89*, 3754–3760. https://doi.org/10.1021/acs.analchem.7b00135.
46. Bai, C., Zhang, J., Qin, Y., Meng, Q., Yao, J., Huang, H., Wei, B., Li, R., Zhang, L., Miao, H., et al. (2022). Strategy for detecting carbon monoxide: Cu^{2+}-assisted fluorescent probe and its applications in biological imaging. Anal. Chem. *94*, 11298–11306. https://doi.org/10.1021/acs.analchem.2c01948.
47. Liu, D., Yang, X., and Wang, B. (2023). Sensing a CO-releasing molecule (CORM) does not equate to sensing CO: the case of DPHP and CORM-3. Anal. Chem. *95*, 9083–9089. https://doi.org/10.1021/acs.analchem.3c01495.
48. Marín-Hernández, C., Toscani, A., Sancenón, F., Wilton-Ely, J.D.E.T., and Martínez-Máñez, R. (2016). Chromo-fluorogenic probes for carbon monoxide detection. Chem. Commun. *52*, 5902–5911. https://doi.org/10.1039/C6CC01335J.
49. Kos, P., and Plenio, H. (2015). Metal complexes of a boron-dipyrromethene (BODIPY)-tagged N-heterocyclic carbene (NHC) as luminescent carbon monoxide chemodosimeters. Chem. Eur. J. *21*, 1088–1095. https://doi.org/10.1002/chem.201405316.

50. Moragues, M.E., Toscani, A., Sancenón, F., Martínez-Máñez, R., White, A. J.P., and Wilton-Ely, J.D.E.T. (2014). A chromo-fluorogenic synthetic "canary" for CO detection based on a pyrenylvinyl ruthenium(II) complex. J. Am. Chem. Soc. *136*, 11930–11933. https://doi.org/10.1021/ja507014a.

51. Baumgartner, L.M., Goryachev, A., Koopman, C.I., Franzen, D., Ellendorff, B., Turek, T., and Vermaas, D.A. (2023). Electrowetting limits electrochemical CO_2 reduction in carbon-free gas diffusion electrodes. Energy Adv. *2*, 1893–1904. https://doi.org/10.1039/D3YA00285C.

52. Quinn, A., Sedev, R., and Ralston, J. (2005). Contact angle saturation in electrowetting. J. Phys. Chem. B *109*, 6268–6275. https://doi.org/10.1021/jp040478f.

53. Sabharwal, M., Pant, L.M., Patel, N., and Secanell, M. (2019). Computational analysis of gas transport in fuel cell catalyst layer under dry and partially saturated conditions. J. Electrochem. Soc. *166*, F3065–F3080. https://doi.org/10.1149/2.0081907jes.

54. Dunwell, M., Lu, Q., Heyes, J.M., Rosen, J., Chen, J.G., Yan, Y., Jiao, F., and Xu, B. (2017). The central role of bicarbonate in the electrochemical reduction of carbon dioxide on gold. J. Am. Chem. Soc. *139*, 3774–3783. https://doi.org/10.1021/jacs.6b13287.

55. Zhu, S., Jiang, B., Cai, W.B., and Shao, M. (2017). Direct observation on reaction intermediates and the role of bicarbonate anions in CO_2 electrochemical reduction reaction on Cu surfaces. J. Am. Chem. Soc. *139*, 15664–15667. https://doi.org/10.1021/jacs.7b10462.